Variational regional inverse modeling of reactive species emissions with PYVAR-CHIMERE-v2019

Audrey Fortems-Cheiney[1], Isabelle Pison[1], Grégoire Broquet[1], Gaëlle Dufour[2], Antoine Berchet[1], Elise Potier[1], Adriana Coman[2], Guillaume Siour[2], and Lorenzo Costantino[2]

[1]Laboratoire des Sciences du Climat et de l'Environnement, LSCE-IPSL (CEA-CNRS-UVSQ), Université Paris-Saclay, 91191 Gif-sur-Yvette, France.

[2]Laboratoire Interuniversitaire des Systèmes Atmosphériques, UMR CNRS 7583, Université Paris Est Créteil et Université Paris Diderot, Institut Pierre Simon Laplace, Créteil, France.

Abstract

Up-to-date and accurate emission inventories for air pollutants are essential for understanding their role in the formation of tropospheric ozone and particulate matter at various temporal scales, for anticipating pollution peaks and for identifying the key drivers that could help mitigate their concentrations. This paper describes the Bayesian variational inverse system PYVAR-CHIMERE, which is now adapted to the inversion of reactive species. Complementarily with bottom-up inventories, this system aims at updating and improving the knowledge on the high spatio-temporal variability of emissions of air pollutants and their precursors. The system is designed to use any type of observations, such as satellite observations or surface station measurements. The potential of PYVAR-CHIMERE is illustrated with inversions of both CO and NO_x emissions in Europe, using the MOPITT and OMI satellite observations, respectively. In these cases, local increments on CO emissions can reach more than +50%, with increases located mainly over Central and Eastern Europe, except in the south of Poland, and decreases located over Spain and Portugal. The illustrative cases for NO_x emissions also lead to large local increments (> 50%), for example over industrial areas (e.g., over the Po Valley) and over the Netherlands. The good behavior of the inversion is shown through statistics on the concentrations: the mean bias, RMSE, standard deviation and correlation between the simulated and observed concentrations. For CO, the mean bias is reduced by about 27% when using the posterior emissions, the RMSE and the standard deviation are reduced by about 50% and the correlation is strongly improved (0.74 when using the posterior emissions against 0.02); for NO_x, the mean bias is reduced by about 24%, the RMSE and the standard deviation are reduced by about 7% but the correlation is not improved. We reported strong non-linear relationships between NO_x emissions and satellite NO_2 columns, now requiring a fully comprehensive scientific study.

1. Introduction

The degradation of air quality is a worldwide environmental problem: 91% of the world's population have breathed polluted air in 2016 according to the World Health Organization (WHO), resulting in 4.2 millions of premature deaths every year [WHO, 2016]. The recent study of Lelieveld et al. [2019] even suggests that the health impacts attributable to outdoor air pollution are substantially higher than previously assumed (with 790,000 premature deaths in the 28 countries of the European Union against the previously estimated 500,000 [EEA, 2018]). The main regulated primary (i.e. directly emitted in the atmosphere) anthropogenic air pollutants are carbon monoxide (CO), nitrogen oxides ($NO_x = NO + NO_2$), sulfur dioxide (SO_2), ammonia (NH_3), volatile organic compounds (VOCs), and primary particles. These primary air pollutants are precursors of secondary (i.e. produced in the atmosphere through chemical reactions) pollutants such as ozone (O_3) and Particulate Matter (PM), which are also threatening to both human health and ecosystems. Monitoring concentrations and quantifying emissions are still challenging and limit our capability to forecast air quality to warn population and to assess i) the exposure of population to air pollution and ii) the efficiency of mitigation policies.

Bottom-up (BU) inventories are built in the framework of air quality policies such as The Convention on Long-Range Transboundary Air Pollution (LRTAP, http://www.unece.org) for air pollutants. Based on national annual inventories, research institutes compile gridded global or regional, monthly inventories (mainly for the US, Europe and China) with a high spatial resolution (currently regional or city scale inventories are typically finer than 0.1°x0.1°). These inventories are constructed by combining available (economic) statistics data from different detailed activity sectors with the most appropriate emission factors (defined as the average emission rate of a given species for a given source or process, relative to the unit of activity in a given administrative area). It is important to note that the activity data (often statistical data) has an inherent uncertainty and that its reliability may vary between countries or regions. In addition, the emission factors bear large uncertainties in their quantification [Kuenen et al., 2014; EMEP/EEA, 2016; Kurokawa et al., 2013]. Moreover, these inventories are often provided at the annual or monthly scale with typical temporal profiles to build the weekly, daily and hourly variability of the emissions. The combination of uncertain activity data, emission factors and emission timing can be a large source of uncertainties, if not errors, for forecasting or analyzing air quality [Menut et al., 2012]. Finally, since updating the inventories and gathering the required data for a given year is costly in time, manpower and money, only a few institutes have offered estimates of the gaseous pollutants for each year since 2011 (i.e, European Monitoring and Evaluation Programme EMEP updated until the year 2017, MEIC updated until the year 2017 to our knowledge). Nevertheless, using knowledge

from inventories and air quality modeling, emissions have been mitigated. For example, from 2010 to nowadays, emissions in various countries have been modified and/or regional trends have been reversed downwards (e.g., the decrease of NO_x emissions over China since 2011 [de Foy et al., 2016]), leading to significant changes in the atmospheric composition. Consequently, the knowledge of precise and updated budgets, together with seasonal, monthly, weekly and daily variations of gaseous pollutants driven, amongst other processes, by the emissions are essential for understanding their role in the formation of tropospheric ozone and PMs at various temporal scales, for anticipating pollution peaks and for identifying the key drivers that could help mitigate these concentrations.

In this context, complementary methods have been developed for estimating emissions using atmospheric observations. They operate in synergy between a chemistry-transport model (CTM) which links the emissions to the atmospheric concentrations, atmospheric observations of the species of interest, and statistical inversion techniques. A number of studies using inverse modeling were first carried out for long-lived species such as greenhouses gases (GHGs) (e.g., carbon dioxide CO_2 or methane CH_4) at the global or continental scales [Hein et al., 1997; Bousquet et al. 1999], using surface measurements. Later, following the development of monitoring station networks, the progress of computing power, and the use of inversion techniques more appropriate to non-linear problems, these methods were applied to shorter-lived molecules such as CO. For these various applications (e.g., for CO_2, CH_4, CO), the quantification of sources was solved at the resolution of large regions [Pétron et al., 2002]. Finally, the growing availability and reliability of observations since the early 2000s (in-situ surface data, remote sensing data such as satellite data), the improvement of the global CTMs, of the computational capacities and of the inversion techniques have increased the achievable resolution of global inversions, up to the global transport model grid cells, i.e. typically with a spatial resolution of several hundreds of square kilometers [Stavrakou and Muller, 2006; Pison et al., 2009; Fortems-Cheiney et al., 2011; Hooghiemstra et al., 2012; Yin et al., 2015; Miyazaki et al., 2017, Zheng et al., 2019].

Today, the scientific and societal issues require an up-to-date quantification of pollutant emissions at a higher spatial resolution than the global one and imply to widely use regional inverse systems. However, although they are suited to reactive species such as CO and NO_x, and their very large spatial and temporal variability, they have hardly been used to quantify pollutant emissions. Some studies inferred NO_x [Pison et al., 2007; Tang et al., 2013] and VOC emissions [Koohkan et al., 2013] from surface measurements. Konovalov et al. [2006, 2008, 2010], Mijling et al. [2012, 2013], van der A et al. [2008], Lin et al. [2012] and Ding et al. [2017] have also shown that satellite

107 observations are a suitable source of information to constrain NO_x emissions. These regional
108 inversions using satellite observations were often based on Kalman Filter (KF) schemes [Mijling et
109 al., 2012, 2013; van der A et al., 2008; Lin et al., 2012; Ding et al., 2017].

110

111 Variational inversion systems allow solving for high dimensional problems, typically solving for
112 the fluxes at high spatial and temporal resolution, which can be critical to fully exploit satellite
113 images. Here, we present the Bayesian variational atmospheric inversion system PYVAR-
114 CHIMERE for the monitoring of anthropogenic emissions of reactive species at the regional scale.
115 It is based on the Bayesian variational assimilation code PYVAR [Chevallier et al. 2005] and on the
116 regional state-of-the-art CTM CHIMERE [Menut et al., 2013; Mailler et al., 2017]. CHIMERE is
117 dedicated to the study of regional atmospheric pollution events [e.g., Ciarelli et al., 2019; Menut et
118 al., 2020], included in the operational ensemble of the Copernicus Atmosphere Monitoring Service
119 (CAMS) regional services. The main strengths of PYVAR-CHIMERE come from the strengths of
120 CHIMERE and from its high modularity for the definition of the control vector. CHIMERE is
121 indeed an extremely flexible code, in particular for the definition of the chemical scheme.
122 The PYVAR-CHIMERE system takes advantage of the previous developments for the
123 quantification of fluxes of long-lived GHG species such as CO_2 [Broquet et al., 2011] and CH_4
124 [Pison et al., 2018] at the regional to the local scales, but now solves for reactive species such as CO
125 and NO_x. It has also a better level of robustness, clarity, portability, and modularity than these
126 previous systems. Variational techniques require the adjoint of the model to compute the sensitivity
127 of simulated atmospheric concentrations to corrections of the fluxes. CHIMERE is one of the few
128 CTMs for which the adjoint has been coded. For global models, they include: GEOS-CHEM
129 [Henze et al., 2007], IMAGES [Stavrakou and Muller, 2006], TM5 [Krol et al., 2008], GELKA
130 [Belikov et al., 2016] and LMDz [Chevallier et al., 2005; Pison et al., 2009] ; for limited-area
131 models they include: CMAQ [Hakami et al., 2007], EURAD-IM [Elbern et al., 2007],
132 RAMS/CTM-4DVAR [Yumimoto et Uno, 2006], WRF-CO2 4D-Var [Zheng et al., 2018]).

133

134 The principle of variational atmospheric inversion and the configuration of PYVAR-CHIMERE are
135 described in Section 2 and in Section 3, respectively. Details about the forward, tangent-linear and
136 adjoint codes of CHIMERE are also given. Then, the potential of PYVAR-CHIMERE is illustrated
137 in Section 4 with the optimization of European CO and NO_x emissions, constrained by observations
138 from the Measurement of Pollution in the Troposphere (MOPITT) and from the Ozone Monitoring
139 Instrument (OMI) satellite instruments, respectively.

140

141

2. Principle of Bayesian variational atmospheric inversion

In what follows, we use the notations and equations used in the inverse modeling community [Rayner et al., 2019]. The Bayesian variational atmospheric inversion method adjusts a set of control parameters, including parameters related to the emissions whose estimate is the primary target of the inversion.

The prior information about the parameters $\mathbf{x}$ to be optimized during the inversion process is given by the vector $\mathbf{x^b}$. The parameters to be optimized can be surface fluxes but may also include initial or boundary conditions for example, as explained in Section 3.4. The adjustments are applied to prior values, usually taken, for the emissions, from pre-existing BU inventories. The principle is to minimize, on the one hand, the departures from the prior estimates of the control parameters, which are weighted by the uncertainties in these estimates (called hereafter "prior uncertainties"), and, on the other hand, the differences between simulated and observed concentrations, which are weighted by all other sources of uncertainties explaining these differences (called hereafter all together "observation errors"). In statistical terms, the inversion searches for the most probable estimate of the control parameters given their prior estimates, observations, CTM and their associated uncertainties. The solution, which will be called posterior estimate, is found by the iterative minimization of a cost function J [Talagrand et al., 1997], defined as:

$$J(\boldsymbol{x}) = \left(\boldsymbol{x} - \boldsymbol{x^b}\right)^T \boldsymbol{B}^{-1}\left(\boldsymbol{x} - \boldsymbol{x^b}\right) + (H(\boldsymbol{x}) - \boldsymbol{y})^T \boldsymbol{R}^{-1}(H(\boldsymbol{x}) - \boldsymbol{y}) \tag{Eq. 1}$$

H is the non-linear observation operator that projects the control vector $\mathbf{x}$ onto the observation space. In most of the variational atmospheric inversion cases (such as those described in Section 4), the observation operator includes the operations performed by the CTM in linking the emissions to the concentrations and any other transformation to compute the simulated equivalent of the observations such as an interpolation or an extraction and averaging of the simulated concentration fields (see Section 3.5). The observations in $\mathbf{y}$ could be surface measurements and/or remote sensing data such as satellite data. The prior uncertainties and the observation errors are assumed to be unbiased and to have a Gaussian distribution. Consequently, the prior uncertainties are characterized by their covariance matrix $\mathbf{B}$ and the observation errors are characterized by their covariance matrix $\mathbf{R}$. By definition, the observation errors combine errors in both the data and the observation operator, in particular measurement errors and errors in the conversion of satellite measurement into concentration data, errors from the CTM, representativity errors due to the comparison between point measurements and gridded models or due to the representation of the fluxes as gridded maps at a given spatial resolution, and aggregation errors associated with the optimization of emissions at a given spatial and/or temporal resolution (as specified in the control vector) that is different from (usually coarser than) that of the CTM [Wang et al., 2017].

177

178   For inversions with observation and control vectors having a high dimension, the minimum of J

179   cannot be found analytically due to computational limitations. It can be reached iteratively with a

180   descent algorithm. In this case, the iterative minimization of J is based on a gradient method. J is

181   calculated with the forward observation operator (including the CTM) and its gradient relative to

182   the control parameters **x** is provided by the adjoint of the observation operator (including the adjoint

183   of the CTM). The gradient is defined as:

184   $\nabla J(\boldsymbol{x}) = \boldsymbol{B}^{-1}(\boldsymbol{x} - \boldsymbol{x}^{\boldsymbol{b}}) + H^{*}\boldsymbol{R}^{-1}(H(\boldsymbol{x}) - \boldsymbol{y})$ (Eq. 2)

185   where H^{*} is the adjoint of the observation operator.

186

187   The high non-linearity of the chemistry for reactive species makes it difficult to use its tangent-

188   linear to approximate the actual observation operator, and, more generally, it makes the inversion

189   problem highly non-linear. Therefore, in PYVAR-CHIMERE, we use the M1QN3 limited memory

190   quasi-Newton minimization algorithm [Gilbert and Lemaréchal, 1989], which relies on the actual

191   CHIMERE non-linear model to compute J at each iteration of the minimization. As most quasi-

192   Newton methods, it requires an initial regularization of **x**, the vector to be optimized, for better

193   efficiency. We adopt the most generally used regularization, made by minimizing in the space

194   defined by:

195   $\chi = \boldsymbol{B}^{\frac{1}{2}}(\boldsymbol{x} - \boldsymbol{x}^{\boldsymbol{b}})$ (Eq. 3)

196   instead of the control space defined by **x**. Although more advanced regularizations can be chosen,

197   the minimization with χ is preferred for its simplifying the equation to solve. In the χ-space,

198   Equation 2 can be re-written as follows:

199   $\nabla J \chi = \chi + \boldsymbol{B}^{\frac{1}{2}}H^{*}(\boldsymbol{R}^{-1}(H(\boldsymbol{x}) - \boldsymbol{y}))$ (Eq. 4)

200

201   The criterion for stopping the algorithm is based on a threshold set on the ratio between the final

202   and initial gradient norms or on the maximum number of iterations to perform. As shown in Figure

203   1, the minimization algorithm repeats the forward-adjoint cycle to get an estimate close to the

204   optimal solution of the inversion problem for the control parameters. This approximation of the

205   optimal estimate is found by satisfying the convergence criteria of the minimizer with a given

206   reduction of the norm of the gradient of J. Nevertheless, due to the non-linearity of the problem, the

207   minimization may reach a local minimum only, instead of the global minimum.

208

209   Finally, the calculation of the uncertainty in the estimate of emissions from the inversion, known as

210   "posterior uncertainty", is challenging in a variational inverse system [Rayner et al., 2019]. Even

211 though the posterior uncertainty can be explicitly written in various analytical forms, it requires the
212 inversion of matrices that are too large to invert given the current computational resources in our
213 variational approach. As a trade-off between computing resources and comprehensiveness, the
214 analysis error may be evaluated by an approach based on a propagation of errors through sensitivity
215 tests (e.g., as in Fortems-Cheiney et al., [2012]). It can also be estimated through a Monte Carlo
216 Ensemble [Chevallier et al., 2007], implemented in PYVAR. Nevertheless, it should be noted that
217 the cost of the Monte Carlo experiments used to derive these posterior uncertainties is huge.
218
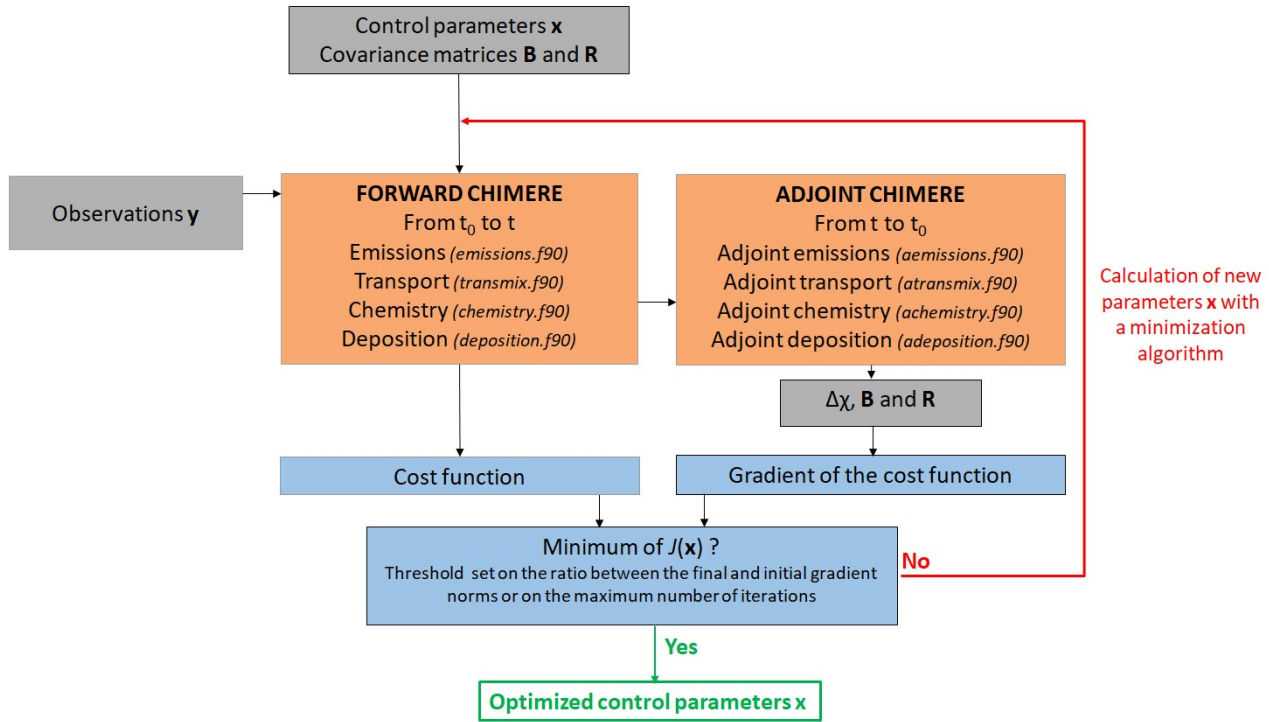
219
220 **Figure 1.** *Simplified scheme of the iterative minimization in PYVAR-CHIMERE. PYVAR,*
221 *CHIMERE and text sources are displayed in blue, in orange and in grey, respectively.*
222

3. The PYVAR-CHIMERE configuration

3.1. PYVAR adapted to CHIMERE

225 The PYVAR-CHIMERE inverse modeling system is based on the Bayesian variational assimilation
226 code PYVAR [Chevallier et al. 2005] and on a previous inversion system coupled to CHIMERE
227 [Pison et al., 2007]. PYVAR is an ensemble of Python scripts, which deals with preparing the
228 vectors and the matrices for the inversion, drives the required Fortran codes of the transport model
229 and computes the minimization of the cost function to solve the inversion. Previously used for
230 global inversions with the LMDz model [e.g., Pison et al., 2009; Chevallier et al., 2010; Fortems-
231 Cheiney et al., 2011; Yin et al., 2015; Locatelli et al., 2015; Zheng et al., 2019], PYVAR has been
232 adapted to CHIMERE with an adjoint code without chemistry by Broquet et al. [2011]. In order to
233 couple PYVAR to the new state-of-the-art version of CHIMERE (see Section 3.2), to include

chemistry, and to increase its modularity, flexibility and clarity, the new system described here has been developed. It includes elements of the inversion system (coded in Fortran90) of Pison et al. [2007].

3.2. Development and parallelization of the adjoint and tangent-linear codes of CHIMERE

To compute the sensitivity of simulated atmospheric concentrations to corrections to the fluxes, the adjoint of CHIMERE has been developed. Originally, the sequential adjoint was coded [Menut et al., 2000; Menut et al., 2003; Pison et al., 2007]. The adjoint has been coded by hand line by line, following the principles formulated by Talagrand [1997]. It contains exactly the same processes as the CHIMERE forward model. The code has been parallelized, which required a redesigning of the entire code, associated with a full testing scheme (see Section 3.3). Furthermore, the tangent-linear (TL) code has been developed and validated (see Section 3.3). Changes have been implemented in the forward CHIMERE code embedded in PYVAR-CHIMERE to match requirements of the studies conducted with this system. These changes have been implemented in both the adjoint and the TL codes. Compared to the CHIMERE 2013 version [Menut et al., 2013], the most important of these changes are, regarding geometry, the possibility of polar domains and the use of the coordinates of the corners of the cells instead of only the centers, allowing the use of irregular grids. Regarding transport, the non-uniform Van Leer transport scheme on the horizontal has been implemented, which is consistent with the use of irregular grids. Finally, various switches have been added to keep the system consistent for GHG studies. For example, we can avoid going into the chemistry, deposition or wet deposition routines when the focused species do not require them (e.g., no chemistry for methane or carbon dioxide at a regional scale).

PYVAR-CHIMERE is currently implemented with a full module of gaseous chemistry. As a compromise between the robustness of the method for reactive species, the time required coding the adjoint and the computational cost with a full chemical scheme, the aerosols modules of CHIMERE have not been included in the adjoint of CHIMERE yet and are therefore not available in PYVAR-CHIMERE. The development and maintenance of the adjoint means that the version used is necessarily one or two versions behind the distributed CHIMERE version (http://www.lmd.polytechnique.fr/chimere/). It should also be noted that PYVAR-CHIMERE only infers anthropogenic emissions at this stage. The optimization of biogenic emissions, which are linearly interpolated at the sub-hourly scale in CHIMERE, is currently under development.

As an example, Figure 2 presents a simplified scheme of how PYVAR scripts are used to drive this version of CHIMERE for forward simulations and inversions using satellite observations.
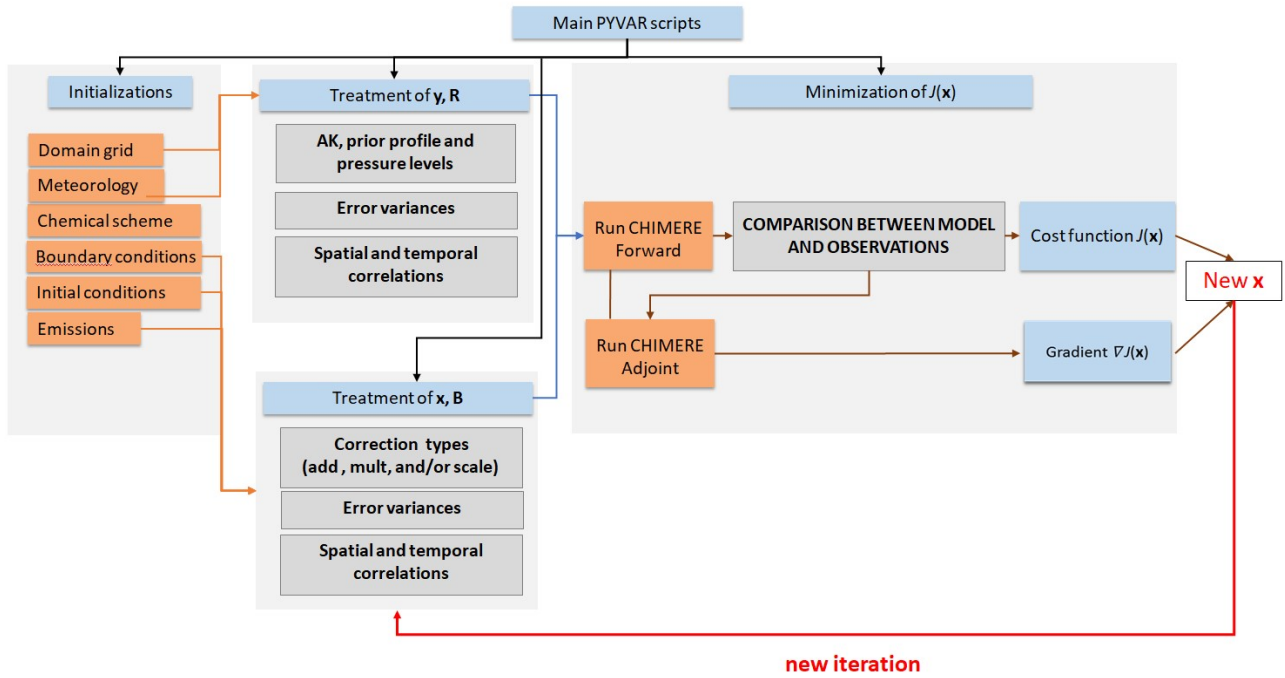
Figure 2. *Simplified scheme of how PYVAR scripts are used to drive CHIMERE for an inversion using satellite observations. PYVAR, CHIMERE and text sources are displayed in blue, in orange and in grey, respectively. "AK" refers to Averaging Kernels as detailed in Section 3.5.*

3.3. Accuracy of tangent-linear and adjoint codes

Different procedures have been implemented to test the accuracy of the TL and adjoint codes. To test the linearity of the TL, we compute a Taylor diagnostic. It consists in computing the TL at $\mathbf{x_0}$ for given increments $\Delta\mathbf{x}$, $dH\mathbf{x_0}(\Delta\mathbf{x})$, then the TL at $\mathbf{x_0}$ for $\lambda \times \Delta\mathbf{x}$ with λ an arbitrary small number, $dH\mathbf{x_0}(\lambda\Delta\mathbf{x})$. Theoretically, if the TL is well coded, $\lambda dH\mathbf{x_0}(\Delta\mathbf{x}) = dH\mathbf{x_0}(\lambda\Delta\mathbf{x})$ by definition. In practice, the difference must be lower than 10 times the precision of the machine on which it is run.

The adjoint code is also tested, by verifying that $<H.\Delta\mathbf{x}, H.\Delta\mathbf{x}> = <\Delta\mathbf{x}, H^T H.\Delta\mathbf{x}>$ where H^T stands for the adjoint at $\mathbf{x}$. What is actually computed is the ratio of the difference between the two scalar products to the second one and the accuracy of the computation. The difference should be a few times the precision of the machine on which it is run.

3.4. Definition of the control vector

The control vector is specified by the user in a text file. This file is formatted following Table 1. The parameters to be inverted may be fluxes and/or initial conditions and/or boundary concentration conditions, at the grid-cell resolution or for one region encompassing up to the whole domain.

291   Several types of corrections can be applied, they are defined in the code as "add", "mult" or "scale".

292   Both the corrections "add" and "mult" are applied to gridded control variables. For correction type

293   "add", the control variables are increments added to the corresponding components of the model

294   inputs. For correction type "mult", the control variables are scaling factors multiplying the

295   corresponding components of the model inputs. The difference between the two options "add" and

296   "mult" plays a role when inverting fluxes which can switch from positive to negative values (like

297   CO_2 natural fluxes). For type "scale", the control variables are scaling factors applied to maps

298   different from the maps of emissions used as prior input of the forward model: for example, activity

299   maps can be used and scaled to get emissions; the obtained values are then added to the

300   corresponding components of the model inputs. With these various types, it is possible to define the

301   control variables as the budgets of emissions for different regions, types of activities, and/or

302   processes, which can thus be directly rescaled by the inversions, similarly to what is done in

303   systems where the control vector is not gridded [Wang et al., 2018]).

304   Different simple but efficient ways of building the error covariance matrix **B** are implemented in

305   PYVAR-CHIMERE. The variances and correlations are defined independently. The variances are

306   specified by the user through standard deviation coefficient (Table 1), which can be a fixed value

307   ("fx") or a percentage ("pc") to define the diagonal standard deviation matrix $\sum$. For correction

308   types "mult" and "scale", as well as for correction type "add" with a fixed value, the value is

309   directly used as the standard deviation of the uncertainty in the corresponding components of the

310   control vector. For correction type "add" with a percentage provided, maps of standard deviation of

311   uncertainty are built by applying this percentage to the matching input fields (fluxes, initial

312   conditions, boundary conditions). The user may also provide a script to build personalized maps of

313   variances.

314

315   Potential correlations between uncertainties in different types of control variables, e.g. between

316   fluxes and boundary conditions, and correlations between uncertainties in different species, e.g.

317   between fluxes of CO and NO_x, are not coded yet. Only correlations for a given type of control

318   variable and a given species are so far taken into account so that the **B** matrix is block diagonal. For

319   a given type of control variable and a given species (in the illustration in section 4.2.2: CO, NO or

320   NO_2 fluxes), spatial and temporal correlations can be defined using correlation lengths through time

321   Lt and space Ls. Those lengths are used to model temporal and/or spatial auto-correlations using an

322   exponentially decaying function: the correlation r between parameters and at a given location but

323   separated by duration $d(x_i, x_j)$, or at a given time but distant by $d(x_i, x_j)$ is given by $r(x_i, x_j) =$

324    $exp\left(\frac{-d(x_i, x_j)}{L}\right)$ $(Eq.\,5)$ where $L = L_T \vee L_S$ is the corresponding correlation length. There is no

325 correlation between uncertainties in land and ocean flux. Note that the spatial correlations are

326 computed for each vertical level independently when dealing with control variables with vertical

327 resolution (3D fields of fluxes when accounting for emission injection heights, or boundary/initial

328 conditions).Vertical correlations in the uncertainties in such variables have not been coded yet.

329 Apart from this, the system assumes that temporal correlations and spatial correlations depend on

330 the time lag and distance but not on the specific time and location of the corresponding parameters.

331 It also assumes that the correlation between uncertainties at different locations and different time

332 can be derived from the product of the corresponding autocorrelation in time and space.

333 Each block of **B** can thus be decomposed based on Kronecker products: $\mathbf{B}=\sum C_t \otimes C_s \sum$ (Eq. 6) where

334 $\otimes$ is the Kronecker product, C_t and C_s are the temporal and spatial correlations, respectively. The

335 calculations involving $\mathbf{B}^{1/2}$ (in Eq. 3, Eq. 4) are simplified in PYVAR-CHIMERE using the Eigen-

336 decomposition of C_t and C_s. Its square root can be calculated according to: $C_t^{1/2}= V_{Ct}D_{Ct}^{1/2}V_{Ct}^{T}$ (Eq.

337 7) (and similarly for C_s), where V_{Ct} is the matrix with the Eigenvectors as columns, and D_{Ct} is the

338 diagonal matrix of Eigenvalues of C_t. It is possible to chose a threshold under which the eigenvalues

339 are truncated when computing the spatial correlations in order to save computation **time** and

340 memory, but not when computing the temporal correlations.

Constrained species	Correction type : - Add - Mult - Scale	Spatial resolution - at the grid-cell resolution - for one region	Temporal resolution (in hours)	Input to constrain: -Fluxes -Initial conditions -Lateral Boundary conditions -Top Boundary conditions	B variance coefficient: -fx -pc	Decorrelation time (in hours)	Decorrelation length on land (in km)	Decorrelation length on sea (in km)
CO	add	0.5°x0.5°	168	Fluxes	100 %	-	-	-
CO	add	0.5°x0.5°	1	Initial conditions	15%	-	-	-
CO	add	0.5°x0.5°	168	Lateral Boundary conditions	15%	-	-	-
CO	add	0.5°x0.5°	168	Top Boundary conditions	15%	-	-	-
NO	add	0.5°x0.5°	24	Fluxes	50 %	-	50	50
NO	add	0.5°x0.5°	1	Initial conditions	15%	-	-	-
NO$_2$	add	0.5°x0.5°	24	Fluxes	50 %	-	50	50
NO$_2$	add	0.5°x0.5°	24	Initial conditions	15%	-	-	-

341 **Table 1**. *Examples for the definition of the control vector and for the construction of the B matrix,*
342 *as illustrated in Section 4.*

343

344 ### 3.5. Equivalents of the observations

345 During forward simulations, the equivalents of the components of **y** (i.e, the equivalents of the
346 individual data) are calculated by PYVAR-CHIMERE. It includes the CTM and an interpolation
347 (see below the vertical interpolation from the model's grid to the satellite levels) or an extraction
348 and averaging (e.g. extracting the grid cell matching the geographical coordinates of a surface
349 station and averaging over one hour). As a compromise between technical issues such as the time
350 required for reading/writing files, the observation operator H that generates the equivalent of the
351 observations by the model (i.e. $H(\mathbf{x})$) has been so far partly embedded in the code of CHIMERE. It
352 makes it easier to use finer time intervals than available in the usual hourly outputs of CHIMERE to
353 compute the required information (e.g., within the finer CTM physical time steps).

354

355 To make comparisons between simulations and satellite observations, the simulated vertical profiles
356 are first interpolated on the satellite's levels (with a vertical interpolation on pressure levels) in
357 CHIMERE. Then, the averaging kernels (AKs), when available, are applied to represent the vertical
358 sensitivity of the satellite retrieval. Two types of formula, depending on the satellite observations
359 used, have been detailed in PYVAR-CHIMERE for the use of AKs: $C_m = AK.C_{m(o)}$ (Eq. 8) or
360 $C_m = x_a + AK(c_{m(o)} - x_a)$ (Eq. 9) where C_m is the modeled column, AK contains the averaging
361 kernels, x_a is the prior profile (provided together with the AKs when relevant) and $C_{m(o)}$ is the
362 vertical distribution of the original model partial columns interpolated to the pressure grid of the
363 AKs.

364

365 ### 3.6. Numerical language

366 The PYVAR code is in Python 2.7, the CHIMERE CTM is coded in Fortran90. The CTM requires
367 several numerical tools, compilers and libraries. The PYVAR-CHIMERE system was developed
368 and tested using the software versions as described in Table 2.

		URL	Version
Software	Python	https://www.python.org/downloads/	2.7
	Fortran compiler ifort	https://software.intel.com/en-us/fortran-compilers	Composer-xe-2013.2.146
Libraries or packages	UnidataNetCDF	https://www.unidata.ucar.edu/	3
	Open MPI	https://www.open-mpi.org/	1.10.5
	GRIB_API	https://confluence.ecmwf.int/display/GRIB/Releases	1.14

| nco | http://nco.sourceforge.net/#Source | 4.6.3 |

Table 2. *URL addresses for the development and the use of the PYVAR-CHIMERE system and its modules.*

PYVAR-CHIMERE's computation time for one node of 10 CPUs is about 4h for 1 day of inversion (with ~10 iterations) for the European domain size of 101 (longitude) x 85 (latitude) x 17 (vertical levels) used in Section 4. The model parallelization results from a Cartesian division of the main geographical domain into several sub-domains, each one being processed by a worker process. To configure the parallel sub-domains, the user has to specify two parameters in the model parameter file: the number of sub-domains for the zonal and meridian directions. The total number of CPUs used is therefore the product of these two numbers plus one for the master process.

4. Potential of PYVAR-CHIMERE for the inversion of CO and NO$_x$ emissions

The potential of the PYVAR-CHIMERE system to invert emissions of reactive species is illustrated with the inversion of CO and NO$_x$ anthropogenic emissions in Europe respectively based on MOPITT CO data and OMI NO$_2$ data. We have chosen to present an illustration of CO inversion over a 7-day window, the first week of March 2015. Considering the short lifetime of NO$_x$ of a few hours [Valin et al., 2013; Liu et al., 2016], we have chosen to present illustration of NO$_x$ inversion over a 1-day window, 19 February 2015. These particular periods have been chosen as they present a representative number of super-observations during winter, and as the emissions are high during that period. All the information required by the system to invert CO and NO$_x$ emissions is listed in Table 1.

4.1. Data and model description

4.1.1. Observations y

We use CO data from the MOPITT instrument [Deeter et al., 2019]. MOPITT has been flown onboard the NASA EOS-Terra satellite, on a low sun-synchronous orbit that crosses the equator at 10:30 and 22:30 LST. The spatial resolution of its observations is about 22x22 km^2 at nadir. It has been operated nearly continuously since March 2000. MOPITT CO products are available in three variants: thermal-infrared TIR only, near-infrared NIR only and the multispectral TIR-NIR product, all containing total columns and retrieved profiles (expressed on a ten-level grid from the surface to 100 hPa). We choose to constrain CO emissions with the MOPITT surface product for our illustration. Among the different MOPITTv8 products, we choose to work with the multispectral MOPITTv8-NIR-TIR one, as it provides the highest number of observations, with a good evaluation against in situ data from NOAA stations [Deeter et al., 2019]. The MOPITTv8-NIR-TIR surface concentrations are sub-sampled into "super-observations" in order to reduce the effect of

errors that are correlated between neighboring observations: we selected the median of each subset of MOPITT data within each 0.5°×0.5° grid-cell and each physical time step (about 5-10 minutes). After this screening, 8437 "super-observations" remain in the 7-day inversion (from 10667 raw observations).It is important to note that the potential of MOPITT to provide information at a high temporal resolution, up to the daily scale, is hampered by the cloud coverage (see the blanks in Figure 5b).

The observational constraint on NO_2 emissions comes from the OMI QA4ECV tropospheric columns [Muller et al., 2016; Boersma et al., 2016, Boersma et al., 2017]. The Ozone Monitoring Instrument (OMI), a near-UV/Visible nadir solar backscatter spectrometer, was launched onboard EOS Aura in July 2004. It has been flown on a 705 km sun-synchronous orbit that crosses the Equator at 13:30 LT. Our data selection follows the criteria of the OMI QA4ECV data quality statement. As the spatial resolution of the OMI data is finer than that of the chosen CHIMERE model grid (13x24 km^2 against 0.5°×0.5°, respectively), the OMI tropospheric columns are sub-sampled into "super-observations" (median of the OMI data within the 0.5°×0.5° grid-cell and each physical time step and its corresponding AK).

4.1.2 CHIMERE set-up

CHIMERE is run over a 0.5°×0.5° regular grid (about 50x50km^2) and 17 vertical layers, from the surface to 200hPa (about 12km), with 8 layers within the first two kilometers. The domain includes 101 (longitude) x 85 (latitude) grid-cells (15.5°W-35°E; 31.5°N-74°N, see Figure 3). CHIMERE is driven by the European Centre for Medium-Range Weather Forecasts (ECMWF) meteorological forecast [Owens and Hewson, 2018]. The chemical scheme used in PYVAR-CHIMERE is MELCHIOR-2, with more than 100 reactions [Lattuati, 1997; CHIMERE 2017], including 24 for inorganic chemistry. The prior anthropogenic emissions for CO and NO_x emissions are obtained from the TNO-GCHco-v1inventory [Super et al., 2020], the last update of the TNO-MACCII inventory [Kuenen et al., 2014]. This inventory is based on the EMEP/Centre on Emission Inventories and Projections (CEIP) official country reporting for air pollutants done in 2017. It is an inventory at 6x6km^2 horizontal resolution. From the annual and national budgets, each sector is assigned to a specific proxy to quantify the spatial variability of the emissions within each country. Temporal profiles are also provided per Gridded Nomenclature For Reporting (GNFR) sector code (variations due to the month, weekday and hour). Following the Generation of European Emission Data for Episodes (GENEMIS) recommendations [Kurtenbach et al., 2001; Aumont et al., 2003], NO_x emissions are speciated as 90% of NO, 9.2% of NO_2, and 0.8% of nitrous acid (HONO). The TNO-GHGco-v1 inventory has been aggregated to the CHIMERE grid.

438

The prior anthropogenic emissions for VOCs are obtained from the EMEP inventory [Vestreng et al., 2005; EMEP/CEIP website]. Biogenic emissions come from the Model of Emissions of Gases and Aerosols from nature (MEGAN) [Guenther et al., 2006]. Different climatological values from the LMDZ-INCA global model [Szopa et al., 2008] or from a Monitoring Atmospheric Composition and Climate (MACC) reanalysis are used to prescribe concentrations at the lateral and top boundaries and the initial atmospheric composition in the domain. Full access to and more information about the MACC reanalysis data can be obtained through the MACC-II web site (http://www.copernicus-atmosphere.eu). In order to ensure realistic fields of simulated CO and NO_2 concentrations from the beginning of the inversion period, runs have been preceded with a 10-day spin-up.

4.1.3. CO Sensitivity to emissions and to initial and boundary conditions

With its lifetime of about two months, CO could be strongly influenced by the initial and lateral boundary conditions prescribed in the CTM. In fact, as seen in Figure 4b, initial and boundary conditions provide a relatively flat background and the patterns which appear clearly over the background are linked to surface emissions (Figure 4a). To characterize the uncertainties in the concentration fields due to the initial and lateral boundary conditions, we performed a sensitivity test by using either climatological values from LMDZ-INCA or a MACC reanalysis: maximum relative differences in concentrations of about 15% over continental land are estimated (Figure 4c). The errors assigned to initial and boundary conditions in Section 4.2.2 are based on this sensitivity test.

458

Figure 3. *Mean CO surface concentrations from the 1st to the 7th, March 2015 simulated by CHIMERE a) with anthropogenic and biogenic emissions, and b) without emissions, in ppbv, at the 0.5°x0.5° grid-cell resolution.*

459
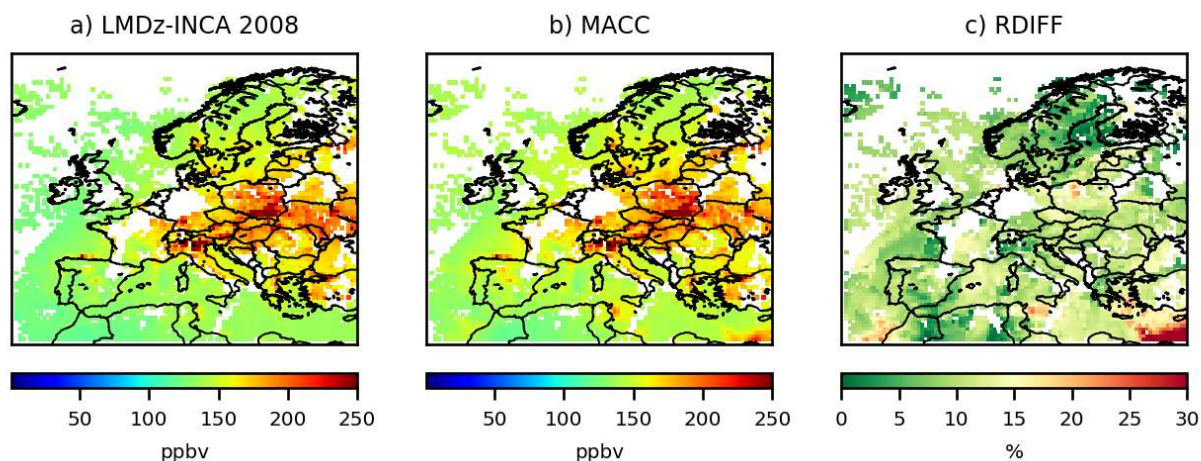
Figure 4. *Mean CO surface concentrations from the 1st to the 7th, March 2015 simulated by CHIMERE using for initial and boundary conditions, a) the climatological values from the LMDZ-INCA global model b) the climatological values from a MACC reanalysis, in ppbv, and c) the relative differences between these two simulations , in %, at the 0.5°x0.5° grid-cell resolution.*

4.1.4. Comparison between CHIMERE and the observations

460 Large discrepancies are found between the MOPITT CO observations (Figure 5b) and the prior
461 simulation by CHIMERE over Europe (Figure 5a). For the first week of March 2015, CO
462 concentrations are generally under-estimated by CHIMERE, particularly over Central and Eastern
463 Europe (excepted in the south of Poland). On the contrary, CO concentrations seem to be over-
464 estimated over Spain and Portugal. Large discrepancies are also found between the OMI NO$_2$ super-
465 observations and the prior simulation by PYVAR-CHIMERE (Figure 6**),** as already noticed by
466 Huijnen et al. [2010], with an inter-comparison of NO$_2$ OMI-DOMINO tropospheric columns with
467 an ensemble of European regional air quality models including CHIMERE. Over Europe, the prior
468 simulation strongly underestimates the tropospheric columns over industrial areas (e.g., over the
469 Netherlands and over Po Valley). These discrepancies might be due to different causes, which can
470 all interact. A source of uncertainties is related to the observations. For example, satellite data inter-
471 comparison studies reveal large differences between different retrievals of the same compound [Qu
472 et al., 2020]. It can be explained by uncertainties from the CTM (e.g., through the underestimation
473 of the atmospheric production or the underestimation of the species lifetime). It could also be
474 explained by an underestimation of the anthropogenic emissions in the BU inventory.

475
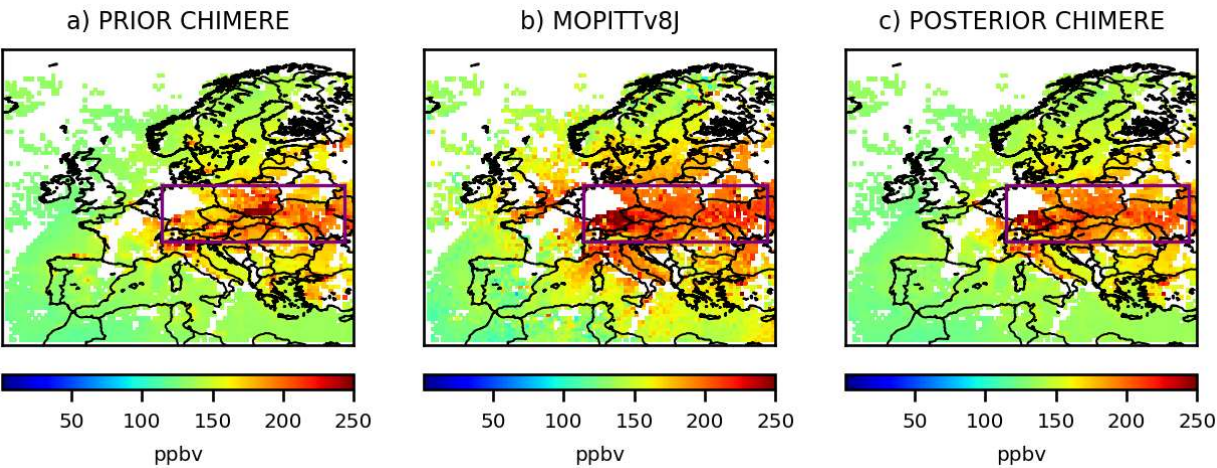
Figure 5. *Mean CO collocated surface concentrations from the 1ˢᵗ to the 7ᵗʰ, March 2015 a) simulated by CHIMERE using the prior TNO-GHGco-v1 emissions and the climatological values from the LMDZ-INCA global model for initial and boundary conditions, b) observed by MOPITTv8-NIR-TIR and c) simulated by CHIMERE using the posterior emissions, in ppbv, at the 0.5°x0.5° grid-cell resolution. Statistics for the comparison between simulations and observations are given in Table 4 for the area in the purple box.*
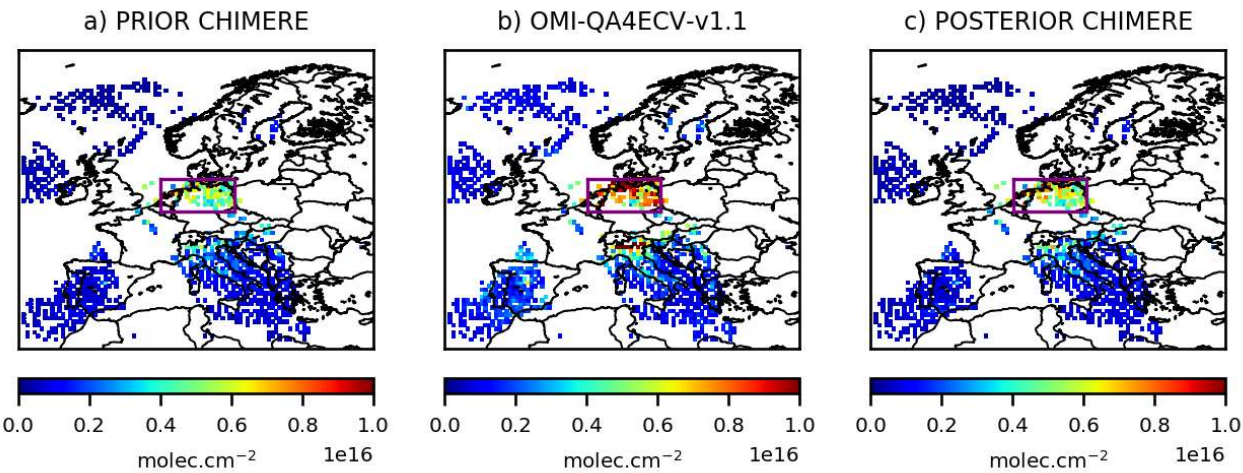
Figure 6. *NO_2 collocated tropospheric columns a) simulated by CHIMERE using the prior TNO-GHGco-v1 emissions and the climatological values from the LMDZ-INCA global model for initial and boundary conditions, b) observed by OMI and c) simulated by CHIMERE using the posterior emissions, in 10^{16} molec.cm⁻², at the 0.5°x0.5° grid-cell resolution, the 19ᵗʰ, February 2015. Statistics for the comparison between simulations and observations are given in Table 5 for the area in the purple box.*

4.2. Inversions

4.2.1. Control vector x

For the CO inversion, the control vector **x** contains:

- the CO anthropogenic emissions at a 7-day temporal resolution, a 0.5° ×0.5° (longitude, latitude) horizontal resolution, and 8 vertical levels, i.e. 101×85×8 components in **x**,
- the CO 3D initial conditions at a 0.5° ×0.5° (longitude, latitude) resolution × 17 vertical levels,
- the CO lateral and top boundary conditions at a 7-day temporal resolution, at a 0.5° ×0.5° (longitude, latitude) resolution, i.e. (2x101 + 2x85) and 17 vertical levels.

Considering its short lifetime, there is no boundary conditions for NO_2. For the NO_x inversion, the control vector **x** contains:

- the NO and NO_2 anthropogenic emissions at a 1-day temporal resolution, at a 0.5° ×0.5° (longitude, latitude) resolution and 8 vertical levels, i.e. 101×85×8 grid cells,
- the NO and NO_2 3D initial conditions at a 0.5° ×0.5° (longitude, latitude) resolution and 17 vertical levels.

4.2.2. Covariance matrices B and R

To our knowledge, there are few available studies dealing with the estimates of the uncertainties in gridded bottom-up emission inventories at the 0.5°x0.5° resolution or higher. The characterization of their statistics in the inversion configuration is consequently often based on crude assumptions from the inverse modelers. Defining the covariance matrices **B** and **R** is not an easy task, while incorrectly specifying these matrices has a very strong impact on the results of the inversion. Especially, the relative weights of **B** and **R**, and the spatial and temporal correlations in B influence the degree of freedom and the structure for the adjustments attempted by the inversion in the optimization process. Consequently, as an example for the NO_x inversion, different sensitivity tests described in Table 3 have been performed for the construction of the **B** matrix. For both the prior NO and NO_2 emissions at 1-day and 0.5° resolution, the prior error standard deviations are first assigned to 50% of the prior estimate of the emissions (test A), as in Souri et al. [2020]. Sensitivity tests have also been performed with prior error standard deviations assigned to 80 and 100% of the prior estimate of the emissions (test C and test D, respectively, Figure 8).

With prior error standard deviations set at 15% of the initial conditions, the changes in initial conditions are very small (not shown) and do not affect the posterior emissions (test B, Figure 8). As indicated in Section 3.4 and in Table 1, it is possible to use correlations in **B**, as in Broquet et al. [2011], in Broquet et al. [2013] and in Kadygrov et al. [2015]. We demonstrate the strong impact of spatial correlations, defined by an e-folding length of 50km over land and over the sea, on our inversions results (test E, Figure 8).

Name of the sensitivity tests	Prior error standard deviations in B		Spatial correlation in B	Number of iterations	Reduction of the norm of the gradient of *J*
	On prior emissions	On prior initial conditions			
A	50%	-	-	4	99%
B	50%	15%	-	6	98%
C	80%	15%	-	7	97%
D	100%	15%	-	6	95%
E	50%	15%	50km	5	92%

Table 3. *Description of the different sensitivity tests performed for the construction of the **B** matrix for the NO$_x$ inversion.*

Even though annual CO emissions in Western Europe may be well known, with uncertainties of 6% according to Super et al., [2020], larger uncertainties could affect Eastern Europe. Moreover, large uncertainties still affect bottom-up emission inventories at the 0.5° resolution: spatial disaggregation of the national scale estimates to provide gridded estimates causes a significant increase in the uncertainty for CO [Super et al., 2020]. For the inversion of CO emissions, the error standard deviations assigned to the prior CO emissions at 7-day and 0.5° resolution are 100%. This value of 100% has already been chosen in Fortems-Cheiney et al. [2011] and in Fortems-Cheiney et al. [2012]. For this CO illustration, the covariance matrix **B** of the prior errors is defined as diagonal (i.e. only variances in the individual control variables listed in 4.2.1 are taken into account).With such a set-up, in theory, we could obtain negative posterior emissions since the inversion system does not impose a constraint of positivity in the results. Nevertheless, even an uncertainty of 100% leads to a prior distribution mostly (>80%) on the positive side. The assimilation of data showing an increase above the background (at the edges of the domain; not shown) further drive the inversion towards positive emissions for both CO and NO$_x$ inversions. In practice, our inversion does not lead to negative posterior emissions (Figure 7b). Spatial and temporal correlations in **B** would further

536   limit the probability to get negative emissions locally by smoothing the posterior emissions at a

537   spatial scale at which the "aggregated" prior uncertainty is smaller than 100%. However, a

538   positivity constraint should be implemented in future versions of the system.

539

540   Based on the sensitivity test in Figure 4, the errors assigned to the CO lateral boundary conditions

541   and to their initial conditions are set at 15%. As these relative errors are significantly lower than

542   those for the emissions and as variations in the CO surface concentrations are mainly driven by

543   emissions (Figure 3), we assume a small relative influence of the correction of initial and boundary

544   conditions on our results. The variance of the individual observation errors in **R** is defined as the

545   quadratic sum of the measurement error reported in the MOPITT and the OMI data sets, and of the

546   CTM errors (including chemistry and transport errors and representativity errors) set at 20% of the

547   retrieval values. The representativity errors could have been reduced with the choice of a finer CTM

548   resolution (e.g., with a resolution closer to the size of the satellite pixel). Error correlations between

549   the super-observations are neglected, so that the covariance matrix **R** of the observation errors is

550   diagonal.

551

4.2.3. Inversion of CO emissions

552

553   Ten iterations are needed to reduce the norm of the gradient of J by 90% with the minimization

554   algorithm M1QN3 and obtain the increments, i.e. the corrections provided by the inversion. The

555   prior CO emissions over Europe for the first week of March 2015 and their increments are shown in

556   Figure 7. As expected from the large differences between the prior surface concentrations (Figure

557   5a) and the MOPITT observations (Figure 5b), local increments can reach more than +50% (Figure

558   7b). CO emissions are increased over Central and Eastern Europe, except in the south of Poland. On

559   the contrary, CO emissions are decreased over Spain and Portugal. The analyzed concentrations are

560   the concentrations simulated by CHIMERE with the posterior fluxes: as expected, the optimization

561   of the fluxes improves the fit of the simulated concentrations to the observations (Figure 5c),

562   particularly over Central and Eastern Europe. Over this area (see the purple box in Figure 5), the

563   mean bias between the simulation and the observations has been reduced by about 27% when using

564   the posterior emissions (mean bias of 11.6 ppbv against 15.9 ppbv with the prior emissions, Table

565   4). The RMSE and the standard deviation have been reduced by about 50% and the correlation has

566   been strongly improved (0.74 when using the posterior emissions against 0.02).

567
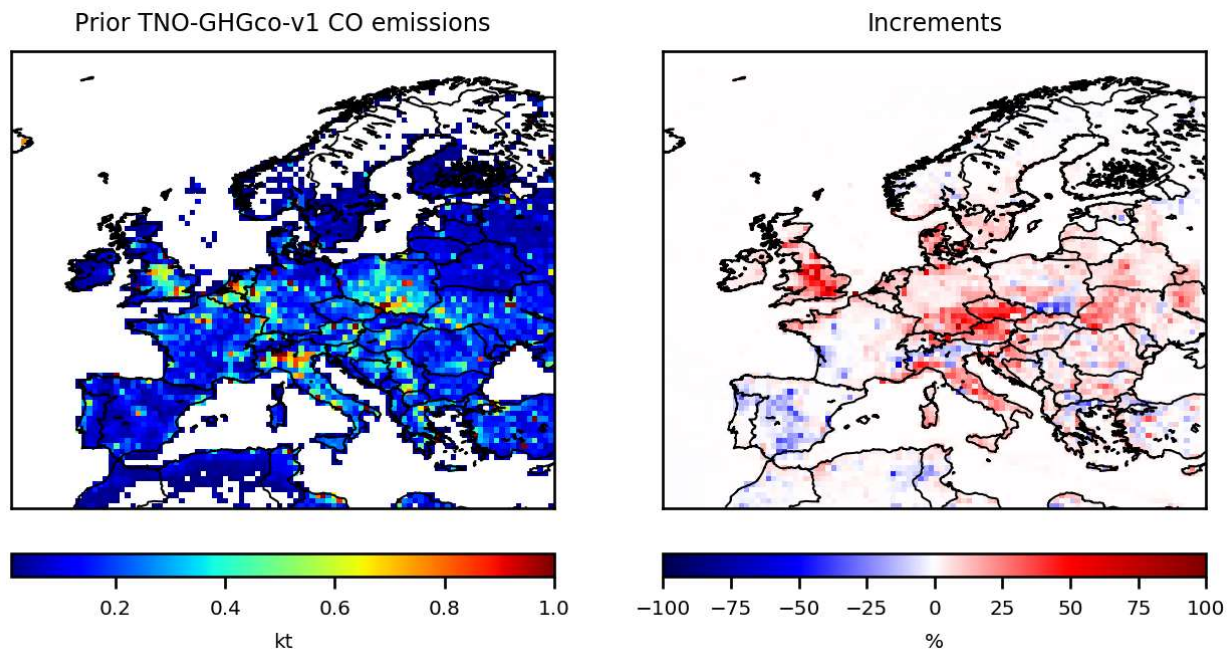
Figure 7. *a) TNO-GHGco-v1 CO anthropogenic prior emissions, in ktCO/grid-cell and b) increments provided by the inversion with constraints from MOPITTv8-NIR-TIR from the 1ˢᵗ to the 7ᵗʰ, March 2015, in %.*

prior				posterior			
MB	RMSE	STD	r	MB	RMSE	STD	r
15.88	41.95	38.82	0.02 (p value = 0.99)	11.58	21.14	17.69	0.74 (p value = 2.08×10^{-11}

Table 4. *Statistics for the comparison between simulated and observed CO surface concentrations over Central and Eastern Europe (see the area in purple in Figure 5). MB= Mean Bias, RMSE= Root Mean Square Error, STD= Standard Deviation are in ppbv. The spatial correlations r are presented with their p value.*

4.2.4. Inversion of NOₓ emissions

The prior NO_x emissions and the corrections provided by the different sensitivity tests of Table 3 are shown in Figure 8. Here, we analyzed the results from inversion E. As expected from the underestimation of the prior tropospheric columns in Figure 6, local increments may be large, for example over industrial areas (e.g., over the Po Valley) and over the Netherlands, with increments of more than +50% (Figure 8b). The analyzed NO_2 tropospheric columns in Figure 6c are the columns simulated by CHIMERE with the NO_2 posterior fluxes: as expected, the optimization of the fluxes improves the fit of the simulated concentrations to the observations over the Netherlands. Over this area (see the purple box in Figure 6), where the OMI uncertainties are lower than 50%

(Figure 9b), the mean bias between the simulation and the observations has been reduced by about 24% when using the posterior emissions (mean bias of 1.9×10^{15} molec.cm^{-2} against 2.6×10^{15} molec.cm^{-2} with the prior emissions, Table 5, Figure 9a). The RMSE and the standard deviation have been reduced by about 7%. The correlation has not been improved.

Even with high emission increments, the impact on the tropospheric columns is rather small. We have performed a test to explain this lack of sensitivity. We have simulated NO$_2$ columns with anthropogenic emissions increased by a factor 3 compared to the simulation in Figure 6a. The ratio between these two simulations shows strong non-linearities, blurring the multiplicative effect of our increments and explaining the lack of sensitivity (not shown). By increasing NO$_x$ anthropogenic emissions, NO$_2$ tropospheric columns can be strongly increased and can even exceed the observations values for particular pixels. NO$_2$ tropospheric columns can also be decreased or only slightly increased. On average, it tends to increase the concentrations by a factor that is much smaller than the factor of increase in the anthropogenic emissions. However, the patterns where the posterior tropospheric columns exceed the observations or, on the opposite are decreased or only slightly increased, explain why the inversion system does not attempt at increasing further the average level of the concentration (to decrease further the general bias to the observations), even though it accounts for the impact of non-linearities in the chemistry through the use of the M1QN3 minimization algorithm. We can conclude that the strong non-linearities of the NO$_x$ chemistry mainly explain the lack of sensitivity between NO$_x$ emissions and satellite NO$_2$ columns. Besides chemical effects, the lack of sensitivity could be also partly due to the contribution of emissions during the preceding days and the assimilation window will be widened in the near future.

The posterior emissions and their uncertainties will have to be evaluated and may bring hints to the cause of the discrepancies between simulated and observed NO$_2$ tropospheric columns. The biases between OMI and simulated NO$_2$ tropospheric columns are a complex topic that is not related to our CHIMERE simulations only [Huijnen et al., 2010; Souri et al., 2020; Elguindi et al., 2020]. Several studies have indeed already reported that strong non-linear relationships exist between NO$_x$ emissions and satellite NO$_2$ columns [Lamsal et al., 2011; Vinken et al., 2014; Miyazaki et al., 2017; Li and Wang, 2019]. This reveals that a fully comprehensive scientific study is required, by analyzing the NO$_x$ lifetime through processes such as the NO$_2$+OH reactions and/or the reactive uptake of NO$_2$ and N$_2$O$_5$ by aerosols [e.g. Lin et al., 2012; Stavrakou et al., 2013].

619
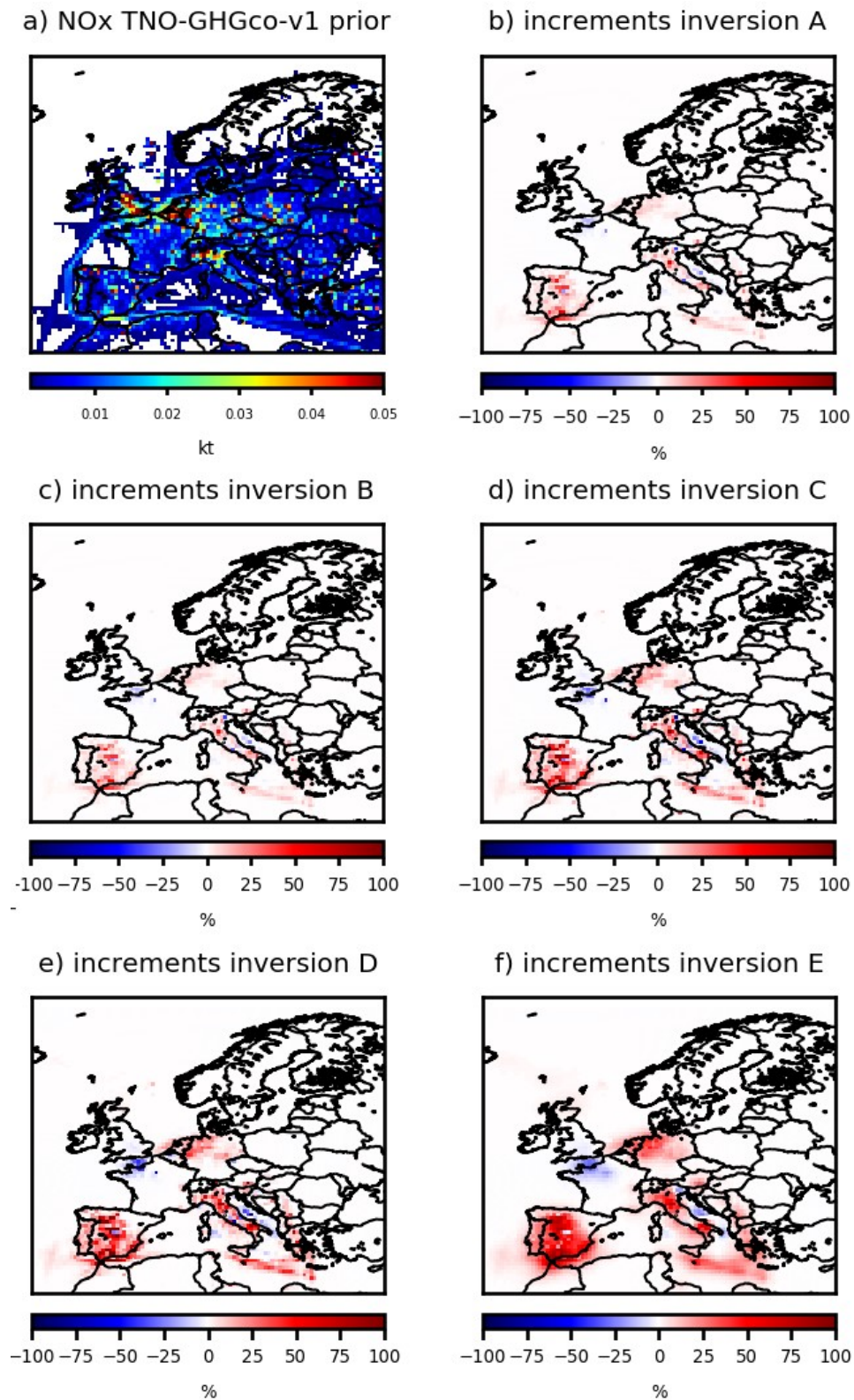
Figure 8. *a) TNO-GHGco-v1 NO$_x$ anthropogenic prior emissions, in ktNO$_2$/grid-cell and*

621 *increments provided by the inversion b) A, c) B, d) C, e) D and f) E with constraints from OMI the*

622 *19th, February 2015, in %. The description of the different inversions is given in Table 3.*

623

624
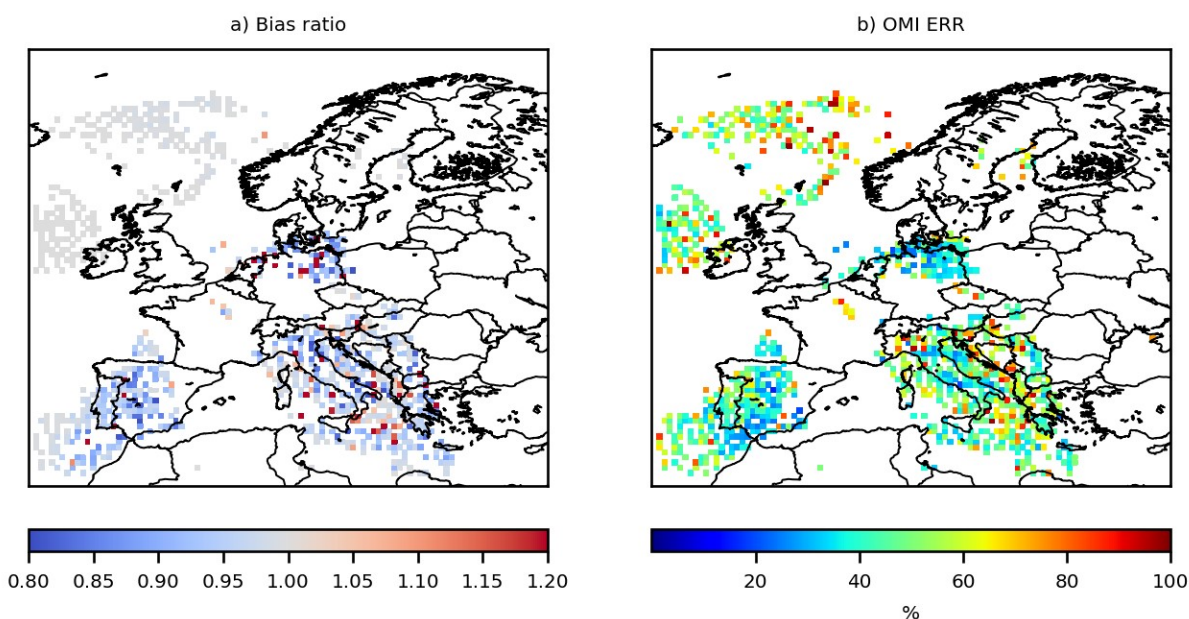
Figure 9. *a) Bias ratio between CHIMERE simulations using the posterior emissions against prior TNO-GHGco-v1 emissions compared to the OMI-QA4ECV-v1.1 observations. All ratios lower than 1, in blue, demonstrate that posterior emissions improve the simulation compared to the prior ones. b) OMI uncertainties, in %, the 19th, February 2015.*

629

	prior				posterior			
	MB	RMSE	STD	r	MB	RMSE	STD	r
NO$_2$	2.6×10^{15}	4.0×10^{15}	3.0×10^{15}	0.008 (p=0.96)	1.9×10^{15}	3.74×10^{15}	2.9×10^{15}	0.01 (p=0.91)

Table 5. *Statistics for the comparison between simulated and observed NO$_2$ tropospheric columns for the inversion E, mainly over the Netherlands (see the area in purple in Figure 6). MB= Mean Bias, RMSE= Root Mean Square Error, STD= Standard Deviation are in molecm.cm^{-2}. The spatial correlations r are presented with their p value.*

5. Conclusion/Discussion

This paper presents the Bayesian variational inverse system PYVAR-CHIMERE, which has been adapted to the inversion of reactive species such as CO and NO$_x$, taking advantage of the previous developments for long-lived species such as CO$_2$ [Broquet et al., 2011] and CH$_4$ [Pison et al., 2018]. We show the potential of PYVAR-CHIMERE, with inversions for CO and NO$_x$ illustrated over Europe. PYVAR-CHIMERE will now be used to infer CO and NO$_x$ emissions over long periods, e.g. first for a whole season or year and then for the recent decade 2005-2015 in the framework of the H2020 VERIFY project over Europe, and in the framework of the ANR PolEASIA project over China, to quantify their trend and their spatio-temporal variability. Nevertheless, as we have reported strong non-linear relationships between NO$_x$ emissions and

satellite NO_2 columns, a fully comprehensive scientific study is required, by analyzing the NO_x lifetime through processes such as the NO_2+OH reactions and/or the reactive uptake of NO_2 and N_2O_5 by aerosols [e.g. Lin et al., 2012; Stavrakou et al., 2013]. Biogenic emissions will be also further studied to better understand the relationship between NO_x emissions and NO_2 spaceborne columns.

The PYVAR-CHIMERE system can handle any large number of both control parameters and observations. It will be able to cope with the dramatic increase in the number of data in the near future with, for example, the high-resolution imaging (pixel of 7x3.5 km^2) of the new Sentinel-5P/TROPOMI program, launched in October 2017. These new space missions with high-resolution imaging have indeed the ambition to monitor atmospheric chemical composition for the quantification of anthropogenic emissions. Moreover, a step forward in the joint assimilation of co-emitted pollutants will be possible with the PYVAR-CHIMERE system and the availability of TROPOMI co-localized images of CO and NO_2. This should improve the consistency of the inversion results and can be used to inform inventory compilers, and subsequently improve emission inventories. Moreover, this development will help in further understanding air quality problems and addressing air quality related emissions at the national to subnational scales.

Author Contribution
All authors have contributed to the manuscript writing (main authors: AFC, GB, IP and GD) and to the development of the present version of the PYVAR-CHIMERE system (main developer: IP). IP and GD have parallelized the adjoint version from Menut et al., [2000], Menut et al., [2003] and Pison et al., [2007]. IP has complemented the adjoint of new parameterizations since the CHIMERE release in 2011 and the tangent-linear model.

Code and Data Availability
OMI QA4ECV NO_2 product can be found here: http://temis.nl/qa4ecv/no2.html.
MOPITTv8-NIR-TIR CO product can be found here: ftp://l5ftl01.larc.nasa.gov/MOPITT/
The CHIMERE code is available here: www.lmd.polytechnique.fr/chimere/.

The associated documentation of PYVAR-CHIMERE is available on the website https://pyvar.lsce.ipsl.fr/doku.php/3chimere:headpage. The documentation includes a whole description of PYVAR-CHIMERE and several tutorials on how to run a first PYVAR-CHIMERE simulation or how to run an inversion.

Competing interests
The authors declare that they have no conflict of interest.

Acknowledgements
We acknowledge L. Menut and C. Schmechtig for their contributions to the development work on the adjoint code of CHIMERE and its parallelization. We acknowledge the TNO team (H.A. Denier

van der Gon, J. Kuenen, S. Dellaert, S.Jonkers, A. Visschedijk, et al.) for providing NO$_x$ and CO emissions over Europe.We also acknowledge the free use of tropospheric NO$_2$ column data from the OMI sensor from http://temis.nl/qa4ecv/no2.htmland the free use of CO surface concentrations from the MOPITT sensor from ftp://l5ftl01.larc.nasa.gov/MOPITT/. For this study, A. Fortems-Cheiney was funded by the French Space Agency-Centre National d'Etudes Spatiales CNES and by the H2020 VERIFY project, funded by the European Commission Horizon 2020 research and innovation programme, under agreement number 776810. L. Costantino was funded by the PolEASIA ANR project under the allocation ANR-15-CE04-0005. This work was granted access to the HPC resources of TGCC under the allocations A0050107232 and A0070102201 made by GENCI. Finally, we wish to thank F. Marabelle (LSCE) and his team for computer support.

References

Aumont, B., Chervier, F., and Laval, S.: Contribution of HONO sources to the NO$_x$/HO$_x$/O$_3$ chemistry in the polluted boundary layer.Atmospheric Environment, 37(4):487 – 498, 2003.

Belikov, D. A., Maksyutov, S., Yaremchuk, A., Ganshin, A., Kaminski, T., Blessing, S., Sasakawa, M., Gomez-Pelaez, A. J., and Starchenko, A.: Adjoint of the global Eulerian–Lagrangian coupled atmospheric transport model (A-GELCA v1.0): development and validation, Geosci. Model Dev., 9, 749-764, https://doi.org/10.5194/gmd-9-749-2016, 2016.

Boersma, K. F., Vinken, G. C. M., and Eskes, H. J.: Representativeness errors in comparing chemistry transport and chemistry climate models with satellite UV–Vis tropospheric column retrievals, Geosci. Model Dev., 9, 875-898, https://doi.org/10.5194/gmd-9-875-2016, 2016.

Boersma, K. F., Eskes, H., Richter, A., De Smedt, I., Lorente, A., Beirle, S., Van Geffen, J., Peters, E., Van Roozendael, M. and Wagner, T.: QA4ECV NO$_2$ tropospheric and stratospheric vertical column data from OMI (Version 1.1) [Data set], Royal Netherlands Meteorological Institute (KNMI), http://doi.org/10.21944/qa4ecv-no2-omi-v1.1, 2017.

Bousquet, P., P. Ciais, P. Peylin, M. Ramonet, and P. Monfray: Inverse modeling of annual atmospheric CO$_2$ sources and sinks: 1. Method and control inversion, *J. Geophys. Res.*, 104(D21), 26,161 – 26,178, doi:10.1029/1999JD900342, 1999.

Broquet, G., Chevallier, F., Rayner, P., Aulagnier, C., Pison, I., Ramonet, M., Schmidt, M., Vermeulen, A. T., and Ciais, P.: A European summertime CO$_2$ biogenic flux inversion at mesoscale from continuous in situ mixing ratio measurements, *J. Geophys. Res.*, 116, D23303, doi: 10.1029/2011JD016202, 2011.

Broquet, G., Chevallier, F., Bréon, F.-M., Kadygrov, N., Alemanno, M., Apadula, F., Hammer, S., Haszpra, L., Meinhardt, F., Morguí, J. A., Necki, J., Piacentino, S., Ramonet, M., Schmidt, M., Thompson, R. L., Vermeulen, A. T., Yver, C., and Ciais, P.: Regional inversion of CO$_2$ ecosystem fluxes from atmospheric measurements: reliability of the uncertainty estimates, Atmos. Chem. Phys., 13, 9039–9056, https://doi.org/10.5194/acp-13-9039-2013, 2013.

Chevallier, F., M. Fisher, P. Peylin, S. Serrar, P. Bousquet, F.-M. Bréon, A. Chédin, and P. Ciais: Inferring CO2 sources and sinks from satellite observations: method and application to TOVS data, *J. Geophys. Res.*, 110, D24309, doi:10.1029/2005JD006390, 2005.

Chevallier, F., F.-M. Bréon, and P. J. Rayner: The contribution of the Orbiting Carbon Observatory to the estimation of CO$_2$ sources and sinks: Theoretical study in a variational data assimilation framework. J. Geophys. Res., 112, D09307, doi:10.1029/2006JD007375, 2007.

Chevallier, F., Ciais, P., Conway, T. J., Aalto, T., Anderson, B. E., Bousquet, P., Brunke, E. G., Ciattaglia, L., Esaki, Y., Fröhlich, M., Gomez, A., Gomez-Pelaez, A. J., Haszpra, L., Krummel, P. B., Langenfelds, R. L., Leuenberger, M., Machida, T., Maignan, F., Matsueda, H., Morguí, J. A., Mukai, H., Nakazawa, T., Peylin, P., Ramonet, M., Rivier, L., Sawa, Y., Schmidt, M., Steele, L. P., Vay, S. A., Vermeulen, A. T., Wofsy, S., and Worthy, D.: CO_2 surface fluxes at grid point scale estimated from a global 21 year reanalysis of atmospheric measurements, J. Geophys. Res., 115, 1–17, https://doi.org/10.1029/2010jd013887, 2010.

Ciarelli, G., Theobald, M. R., Vivanco, M. G., Beekmann, M., Aas, W., Andersson, C., Bergstrom, R., Manders-Groot, A., Couvidat, F., Mircea, M., Tsyro, S., Fagerli, H., Mar, K., Raffort, V., Roustan, Y., Pay, M.-T., Schaap, M., Kranenburg, R., Adani, M., Briganti, G., Cappelletti, A., D'Isidoro, M., Cuvelier, C., Cholakian, A., Bessagnet, B., Wind, P., and Colette, A.: Trends of inorganic and organic aerosols and precursor gases in Europe: insights from the EURODELTA multi-model experiment over the 1990-2010 period, Geosci. Model Dev., 12, 4923-4954, https://doi.org/10.5194/gmd-12-4923-2019, 2019.

CHIMERE documentation, https://www.lmd.polytechnique.fr/chimere/docs/CHIMEREdoc2017.pdf, Last update of this documentation: June 8, 2017,2017.

Deeter, M. N., Edwards, D. P., Francis, G. L., Gille, J. C., Mao, D., Martínez-Alonso, S., Worden, H. M., Ziskin, D., and Andreae, M. O.: Radiance-based retrieval bias mitigation for the MOPITT instrument: the version 8 product, Atmos. Meas. Tech., 12, 4561–4580, https://doi.org/10.5194/amt-12-4561-2019, 2019.

Ding, J., Miyazaki, K., van der A, R. J., Mijling, B., Kurokawa, J.-I., Cho, S., Janssens-Maenhout, G., Zhang, Q., Liu, F., and Levelt, P. F.: Intercomparison of NO$_x$ emission inventories over East Asia, *Atmos. Chem. Phys*., 17, 10125-10141, https://doi.org/10.5194/acp-17-10125-2017, 2017.

EEA, Air quality in Europe - 2018 report, 12/2018, https://www.eea.europa.eu/publications/air-quality-in-europe-2018.

Elbern, H., Strunk, A., Schmidt, H., and Talagrand, O.: Emission rate and chemical state estimation by 4-dimensional variational inversion, Atmos. Chem. Phys., 7, 3749-3769, https://doi.org/10.5194/acp-7-3749-2007, 2007.

Elguindi, N., Granier, C., Stavrakou, T., Darras, S., Bauwens, M., Cao, H., et al.: Intercomparison of magnitudes and trends in anthropogenic surface emissions from bottom-up inventories, top-down estimates, and emission scenarios. Earth's Future, 8, e2020EF001520. https://doi.org/10.1029/2020EF001520, 2020.

EMEP/EEA air pollutant emission inventory guidebook, 2016.

EMEP/CEIP,

https://ceip.at/ms/ceip_home1/ceip_home/webdab_emepdatabase/emissions_emepmodels/

de Foy, B., Lu. Z. and Streets, D.G.: Satellite NO_2 retrievals suggest China has exceeded its NOx reduction goals from the twelfth Five-Year Plan, *Nature Scientific Reports*, 6:35912, 2016.

Fortems-Cheiney, A., et al: Ten years of CO emissions as seen from MOPITT, Journal of Geophysical Research, 116, D5, https://doi.org/10.1029/2010JD014416, 2011.

Fortems-Cheiney, A., Chevallier, F., Pison, I., Bousquet, P., Saunois, M., Szopa, S., Cressot, C., Kurosu, T. P., Chance, K., and Fried, A.: The formaldehyde budget as seen by a global-scale multi-constraint and multi-species inversion system, Atmos. Chem. Phys., 12, 6699–6721, https://doi.org/10.5194/acp-12-6699-2012, 2012.

Gilbert, J., and C. Lemaréchal (1989), Some numerical experiments with variable storage quasi Newton algorithms,Math. Program., 45, 407–435.

Guenther, A., Karl, T., Harley, P., Wiedinmyer, C., Palmer, P. I., and Geron, C.: Estimates of global terrestrial isoprene emissions using MEGAN (Model of Emissions of Gases and Aerosols from Nature), Atmos. Chem. Phys., 6, 3181–3210, https://doi.org/10.5194/acp-6-3181-2006, 2006.

Hakami, A., Henze, D. K., Seinfeld, J. H., Singh, K., Sandu, A., Kim, S., Byun, D., and Li, Q.: The adjoint of CMAQ, Environ. Sci. Technol., 41, 7807–7817, https://doi.org/10.1021/es070944p, 2007.

Hein, R., et coll.: An inverse modeling approach to investigate the global atmospheric methane cycle, *Global. Biogeochem.Cycles*, 11, 43-76, 1997.

Henze, D. K., Hakami, A., and Seinfeld, J. H.: Development of the adjoint of GEOS-Chem, Atmos. Chem. Phys., 7, 2413–2433, https://doi.org/10.5194/acp-7-2413-2007, 2007.

Huijnen, V., Eskes, H. J., Poupkou, A., Elbern, H., Boersma, K. F., Foret, G., Sofiev, M., Valdebenito, A., Flemming, J., Stein, O., Gross, A., Robertson, L., D'Isidoro, M., Kioutsioukis, I., Friese, E., Amstrup, B., Bergstrom, R., Strunk, A., Vira, J., Zyryanov, D., Maurizi, A., Melas, D., Peuch, V.-H., and Zerefos, C.: Comparison of OMI NO_2 tropospheric columns with an ensemble of global and European regional air quality models, Atmos. Chem. Phys., 10, 3273–3296, https://doi.org/10.5194/acp-10-3273-2010, 2010.

Hooghiemstra, P. B., Krol, M. C., Bergamaschi, P., de Laat, A. T. J., van der Werf, G. R., Novelli, P.C., Deeter, M. N., Aben, I., and Rockmann, T.: Comparing optimized CO emission estimates usingMOPITT or NOAA surface network observations, *J. Geophys. Res.*, 117, D06309,doi:10.1029/2011JD017043, 2012.

Kadygrov, N., Broquet, G., Chevallier, F., Rivier, L., Gerbig, C., and Ciais, P.: On the potential of the ICOS atmospheric CO_2 measurement network for estimating the biogenic CO_2budget of Europe, Atmos. Chem. Phys., 15, 12765–12787, https://doi.org/10.5194/acp-15-12765-2015, 2015.

Konovalov, I. B. et coll.: Inverse modelling of the spatial distribution of NO emissions on a continental scale using satellite data, *Atmos. Chem. Phys.*, 6, 1747-1770, doi:10.5194/acp-6-1747-2006, 2006.

Konovalov, I. B., Beekmann, M., Burrows, J. P., and Richter, A.: Satellite measurement based estimates of decadal changes in European nitrogen oxides emissions, *Atmos. Chem. Phys.*, 8, 2623-2641, doi:10.5194/acp-8-2623-2008, 2008.

Konovalov, I. B., Beekmann, M., Richter, A., Burrows, J. P., and Hilboll, A.: Multi-annual changes of NO_x emissions in megacity regions: nonlinear trend analysis of satellite measurement based estimates, *Atmos. Chem. Phys.*, 10, 8481-8498, doi:10.5194/acp-10-8481-2010, 2010.

Koohkan, M. R., Bocquet, M., Roustan, Y., Kim, Y., and Seigneur, C.: Estimation of volatile organic compound emissions for Europe using data assimilation, *Atmos. Chem. Phys.*, 13, 5887-5905, https://doi.org/10.5194/acp-13-5887-2013, 2013.

Krol, M. C., Meirink, J. F., Bergamaschi, P., Mak, J. E., Lowe, D., Jöckel, P., Houweling, S., and Röckmann, T.: What can 14CO measurements tell us about OH?, Atmospheric chemistry and physics, 8, 5033–5044, 2008.

Kuenen, J. J. P., Visschedijk, A. J. H., Jozwicka, M., and Denier van der Gon, H. A. C.: TNO-MACC_II emission inventory; a multi-year (2003–2009) consistent high-resolution European emission inventory for air quality modelling, Atmos. Chem. Phys., 14, 10963-10976, https://doi.org/10.5194/acp-14-10963-2014, 2014.

Kurokawa, J., Ohara, T., Morikawa, T., Hanayama, S., Janssens-Maenhout, G., Fukui, T., Kawashima, K., and Akimoto, H.: Emissions of air pollutants and greenhouse gases over Asian regions during 2000–2008: Regional Emission inventory in ASia (REAS) version 2, *Atmos. Chem. Phys.*, 13, 11019-11058, doi:10.5194/acp-13-11019-2013, 2013.

Kurtenbach, R., Becker, K., Gomes, J., Kleffmann, J., LŽrzer, J., Spittler, M.,Wiesen, P., Ackermann, R., Geyer, A., and Platt, U.: Investigations of emissions and heterogeneousformation of HONO in a road traffic tunnel.Atmospheric Environment, 35(20):9506 – 9517. 3385Ð3394, 2001.

Lamsal, L. N., Martin, R. V., Padmanabhan, A., van Donkelaar, A., Zhang, Q., Sioris, C. E., Chance, K., Kurosu, T. P., and Newchurch, M. J.: Application of satellite observations for timely updates to global anthropogenic NO_x emission inventories, *Geophys. Res. Lett.*, 38, L05810, doi:10.1029/2010GL046476, 2011.

Lattuati, M., Impact des émissions européennes sur le bilan de l'ozone troposphérique a l'interface de l'europe et de l'atlantique nord : apport de la modélisation lagrangienne et des mesures en altitude, Ph.D. thesis, Université Paris VI, 1997.

Lelieveld, J., Klingmüller, K., Pozzer, A., Pöschl, U., Fnais, M., Daiber, A., Münzel, T.; Cardiovascular disease burden from ambient air pollution in Europe reassessed using novel hazard ratio functions, *European Heart Journal*, , ehz135, https://doi.org/10.1093/eurheartj/ehz135, 2019.

Li, J. and Wang, Y.: Inferring the anthropogenic NO_x emission trend over the United States during 2003–2017 from satellite observations: was there a flattening of the emission trend after the Great Recession?, Atmos. Chem. Phys., 19, 15339–15352, https://doi.org/10.5194/acp-19-15339-2019, 2019.

Lin, J.-T., McElroy, M. B., and Boersma, K. F.: Constraint of anthropogenic NO_x emissions in China from different sectors: a new methodology using multiple satellite retrievals, *Atmos. Chem. Phys.*, 10, 63-78, doi:10.5194/acp-10-63-2010, 2010.

Lin, J.-T., Liu, Z., Zhang, Q., Liu, H., Mao, J., and Zhuang, G.: Modeling uncertainties for tropospheric nitrogen dioxide columns affecting satellite-based inverse modeling of nitrogen oxides emissions, Atmos. Chem. Phys., 12, 12255–12275, https://doi.org/10.5194/acp-12-12255-2012, 2012.

Liu, F., Beirle, S., Zhang, Q., Dörner, S., He, K., and Wagner, T.: NO_x lifetimes and emissions of cities and power plants in polluted background estimated by satellite observations, Atmos. Chem. Phys., 16, 5283–5298, https://doi.org/10.5194/acp-16-5283-2016, 2016.

Locatelli, R., Bousquet, P., Saunois, M., Chevallier, F., and Cressot, C.: Sensitivity of the recent methane budget to LMDz sub-grid-scale physical parameterizations, Atmos. Chem. Phys., 15, 9765-9780, https://doi.org/10.5194/acp-15-9765-2015, 2015.

Mailler S., L. Menut, D. Khvorostyanov, M. Valari, F. Couvidat, G. Siour, S. Turquety, R. Briant, P. Tuccella, B. Bessagnet, A. Colette, L. Letinois, and F. Meleux, CHIMERE-2017: from urban to hemispheric chemistry-transport modeling ,*Geosci. Model Dev*., 10, 2397-2423, https://doi.org/10.5194/gmd-10-2397-2017, 2017.

Menut, L., R. Vautard, M. Beekmann, and C. Honoré: Sensitivity of photochemical pollution using the adjoint of a simplified chemistry-transport model, *J. Geophys. Res.*, 105, 15,379–15,402, 2000.

Menut L.: Adjoint modelling for atmospheric pollution processes sensitivity at regional scale during the ESQUIF IOP2, Journal of Geophysical Research - Atmospheres, 108, D17, https://doi.org/10.1029/2002JD002549, 2003.

Menut, L., Goussebaile, A., Bessagnet, B., Khvorostiyanov, D., and Ung, A.: Impact of realistic hourly emissions profiles on air pollutants concentrations modelled with CHIMERE, Atmospheric Envioment, 49, 233–244, doi:10.1016/j.atmosenv.2011.11.057, 2012.

Menut, L., Bessagnet, B., Khvorostyanov, D., Beekmann, M., Blond, N., Colette, A., Coll, I., Curci, G., Foret, G., Hodzic, A., Mailler, S., Meleux, F., Monge, J.-L., Pison, I., Siour, G.,Turquety, S., Valari, M., Vautard, R., and Vivanco, M. G.: CHIMERE 2013: a model for regional atmospheric composition modelling, *Geosci. Model Dev*., 6, 981–1028, doi:10.5194/gmd-6-981-2013, 2013.

Menut, L., Bessanet, B., Siour, G., Mailler, S., Pennel, R. and Cholakian, A. : Impactof lockdown measures to combat Covid-19 on air quality over western Europe, Science of The Total Environment, 741,https://doi.org/10.1016/j.scitotenv.2020.140426, 2020.

Mijling, B., and R. J. van der A: Using daily satellite observations to estimate emissions of short-lived air pollutants on a mesoscopic scale, *J. Geophys. Res.*, 117, D17302, doi:10.1029/2012JD017817, 2012.

Mijling, B., et al., Regional nitrogen oxides emission trends in East Asia observed from space, *Atmos. Chem. Phys.*, 3, 12003, 2013.

Miyazaki, K., Eskes, H., Sudo, K., Boersma, K. F., Bowman, K., and Kanaya, Y.: Decadal changes in global surface NO_x emissions from multi-constituent satellite data assimilation, Atmos. Chem. Phys., 17, 807–837, https://doi.org/10.5194/acp-17-807-2017, 2017.

Muller, J.-P., Kharbouche, S., Gobron, N., Scanlon, T., Govaerts, Y., Danne, O., Schultz, J., Lattanzio, A., Peters, E., De Smedt, I., Beirle, S., Lorente, A., Coheur, P. F., George, M., Wagner, T., Hilboll, A., Richter, A., Van Roozendael, M., and Boersma, K. F.: Recommendations (scientific) on best practices for retrievals for Land and Atmosphere ECVs (QA4ECV Deliverable 4.2 version 1.0), 186 pp., available at: http://www.qa4ecv.eu/sites/default/ files/D4.2.pdf (last access: 12 April 2018), 2016.

Owens, R. G. and Hewson, T.: ECMWF Forecast User Guide, Reading, https://doi.org/10.21957/m1cs7h,https://software.ecmwf.int/wiki/display/FUG/Forecast+User+Guide, 2018.

Pétron, G., Granier, C., Khattatov, B., Lamarque, J.F., Yudin, V., Muller, J.F. and Gille, J.: Inverse modeling of carbon monoxide surface emissions using CMDL networks observations, *J. Geophys. Res,* 107, D24, 2002.

Pison, I., Menut, L., and Bergametti, G.: Inverse modeling of surface NOx anthropogenic emission fluxes in the Paris area during the ESQUIF campaign, *J. Geophys. Res. Atmos.*, 112, D24302, doi:10,1029/2007JD008871, 2007.

Pison, I.,Bousquet, P., Chevallier, F., Szopa, S., and Hauglustaine, D.: Multi-species inversion of CH_4, CO and H_2 emissions from surface measurements, *Atmospheric Chemistry and Physics*, 9, 5281-5297, 2009.

Pison, I., Berchet, A., Saunois, M., Bousquet, P., Broquet, G., Conil, S., Delmotte, M., Ganesan, A., Laurent, O., Martin, D., O'Doherty, S., Ramonet, M., Spain, T. G., Vermeulen, A., and Yver Kwok, C.: How a European network may help with estimating methane emissions on the French national scale, Atmos. Chem. Phys., 18, 3779–3798, https://doi.org/10.5194/acp-18-3779-2018, 2018.

Qu, Z., Henze, D. K., Cooper, O. R., and Neu, J. L.: Improving NO_2 and ozone simulations through global NO_x emission inversions, Atmos. Chem. Phys. Discuss., https://doi.org/10.5194/acp-2020-307, in review, 2020.

Rayner, P. J., Michalak, A. M., and Chevallier, F.: Fundamentals of data assimilation applied to biogeochemistry, Atmos. Chem. Phys., 19, 13911–13932, https://doi.org/10.5194/acp-19-13911-2019, 2019.

Souri, A. H., Nowlan, C. R., González Abad, G., Zhu, L., Blake, D. R., Fried, A., Weinheimer, A. J., Wisthaler, A., Woo, J.-H., Zhang, Q., Chan Miller, C. E., Liu, X., and Chance, K.: An inversion of NO_x and non-methane volatile organic compound (NMVOC) emissions using satellite observations during the KORUS-AQ campaign and implications for surface ozone over East Asia, Atmos. Chem. Phys., 20, 9837–9854, https://doi.org/10.5194/acp-20-9837-2020, 2020.

Stavrakou, T. and J.-F. Müller: Grid-based versus big region approach for inverting CO emissions using Measurement of Pollution in the Troposphere (MOPITT) data, *Journal of Geophysical Research: Atmospheres*,111, D15, 2006.

Stavrakou, T., Muller, J.-F., Boersma, K. F., De Smedt, I., and van der A, R. J.: Assessing the distribution and growthrates of NOx emission sources by inverting a 10-year record of NO_2 satellite columns, *Geophys. Res. Lett.*, 35, 1–5, doi:10.1029/2008GL033521, 2008.

Stavrakou, T., Müller, J.-F., Boersma, K. F., van der A, R. J., Kurokawa, J., Ohara, T., and Zhang, Q.: Key chemical NO_xsink uncertainties and how they influence top-down emissions of

985 nitrogen oxides, Atmos. Chem. Phys., 13, 9057–9082, https://doi.org/10.5194/acp-13-9057-2013,
986 2013.
987
988 Super, I., Dellaert, S. N. C., Visschedijk, A. J. H., and Denier van der Gon, H. A. C.:
989 Uncertainty analysis of a European high-resolution emission inventory of CO_2 and CO to support
990 inverse modelling and network design, Atmos. Chem. Phys., 20, 1795–1816,
991 https://doi.org/10.5194/acp-20-1795-2020, 2020.
992
993 Szopa, S., Foret, G., Menut, L., and Cozic, A.: Impact of large scale circulation on
994 European summer surface ozone: consequences for modeling, *Atmospheric Environment*, 43, 1189–
995 1195,doi:10.1016/j.atmosenv.2008.10.039, 2008.
996
997 Talagrand, O. : Assimilation of observations : an introduction, J. Met. Soc., Japan, 75,
998 191-209, 1997.
999
1000 Tang, X., ZhuJ.,WangZ.F., WangM., GbaguidiA., LiJ., ShaoM., TangG. Q., and JiD.S.:
1001 Inversion of CO emissions over Beijing and its surrounding areas with ensemble Kalman filter,
1002 Atmospheric Environment,81, 676-686, 2013.
1003
1004 Valin, L. C., Russell, A. R., and Cohen, R. C.: Variations of OH rad-ical in an urban
1005 plume inferred from NO_2 column measurements, Geophys. Res. Lett., 40, 1856–1860,
1006 doi:10.1002/grl.50267, 2013.
1007
1008 van der A, R. J., Eskes, H. J., Boersma, K. F., van Noije, T. P. C., van Roozendael, M., De
1009 Smedt, I., Peters, D. H. M. U., and Meijer, E. W.: Trends, seasonal variability and dominant NOx
1010 source derived from a ten year record of NO_2 measured from space, *J. Geophys. Res*., 113, 1–12,
1011 doi:10.1029/2007JD009021, 2008.
1012
1013 Vestreng, V., Breivik, K., Adams, M., Wagner, A., Goodwin, J., Rozovskaya, O.,
1014 andOacyna, J.: Inventory Review 2005 - Emission Data reported to CLRTAP and under the NEC
1015 Direc-tive - Initial review for HMs and POPs .EMEP Status report, Norwegian Meteorological
1016 Institute, Oslo, 2005.
1017
1018 Vinken, G. C. M., Boersma, K. F., Maasakkers, J. D., Adon, M., and Martin, R. V.:
1019 Worldwide biogenic soil NO_x emissions inferred from OMI NO_2 observations, Atmos. Chem.
1020 Phys., 14, 10363–10381, https://doi.org/10.5194/acp-14-10363-2014, 2014.
1021
1022 Yin, Y., Chevallier, F., Ciais, P., Broquet, G., A. Fortems-Cheiney, Pison, I. and Saunois,
1023 M: Decadal trends in global CO emissions as seen by MOPITT, *Atmos. Chem. Phys*., 15, 13433-
1024 13451, 2015.
1025
1026 Yumimoto, K. and Uno, I.: Adjoint inverse modeling of CO emissions over Eastern Asia
1027 using four-dimensional variational data assimilation, Atmospheric Environment, 40, 35, 6836-6845,
1028 DOI: 10.1016/j.atmosenv.2006.05.042, 2006.
1029
1030 Wang, Y., G. Broquet, P. Ciais, F. Chevallier, F. Vogel, N. Kadygrov, L. Wu, Y. Yin, R.
1031 Wang and S. Tao: Estimation of observation errors for large-scale atmospheric inversion of
1032 CO_2emissions from fossil fuel combustion, Tellus B: Chemical and Physical Meteorology, 69:1,
1033 DOI: 10.1080/16000889.2017.1325723, 2017.
1034
1035 Wang, Y., Broquet, G., Ciais, P., Chevallier, F., Vogel, F., Wu, L., Yin, Y., Wang, R., and
1036 Tao, S.: Potential of European [14]CO_2 observation network to estimate the fossil fuel CO_2 emissions

via atmospheric inversions, Atmos. Chem. Phys., 18, 4229–4250, https://doi.org/10.5194/acp-18-4229-2018, 2018.

WHO World Health Organization: Ambient Air Pollution: a global assessment of exposure and burden of disease, 2016.

Zheng, T., French, N. H. F., and Baxter, M.: Development of the WRF-CO2 4D-Var assimilation system v1.0, Geosci. Model Dev., 11, 1725–1752, https://doi.org/10.5194/gmd-11-1725-2018, 2018.

Zheng, B., Chevallier, F., Yin, Y., Ciais, P., Fortems-Cheiney, A., Deeter, M. N., Parker, R. J., Wang, Y., Worden, H. M., and Zhao, Y.: Global atmospheric carbon monoxide budget 2000–2017 inferred from multi-species atmospheric inversions, Earth Syst. Sci. Data, 11, 1411–1436, https://doi.org/10.5194/essd-11-1411-2019, 2019.